JOURNAL OF THERMOPHYSICS AND HEAT TRANSFER
Vol. 17, No. 3, July–September 2003

Construction and Validation of a Dense Gas Shock Tube

Stephen Fergason*
The Aerospace Corporation, Los Angeles, California 90009-2957
Alberto Guardone†
Politecnico de Milano, 20156 Milano, Italy
and
Brian Argrow‡
University of Colorado, Boulder, Colorado 80903-0429

Results from initial tests of a shock tube designed to verify the nonclassical dynamics of Bethe–Zel'dovich–Thompson (BZT) fluids are presented. These tests employed nitrogen at pressures and temperatures required for shock-tube initial conditions that will produce nonclassical phenomena in a BZT fluid. A single-diaphragm, stainless steel shock tube is enclosed in a resistance-heated tube furnace. Each of the 16 segments of the furnace is controlled by a proportional integral differential loop to sustain a uniform temperature along the tube. Water-cooled static and dynamic pressure transducers and thermocouples are used to monitor the static initial conditions and the dynamic wave field. The nitrogen test cases are compared to the ideal gas Riemann problem. The pressure differential of the incident expansion wave matches the theoretical magnitude to within 2%, whereas the average wave speed agrees within 7%. Results of numerical experiments that focus on simulating the diaphragm bursting dynamics are presented. These simulations give an indication of how diaphragm petaling alters the shape of the measured expansion profile with little effect on the overall magnitudes.

Nomenclature

a	=	speed of sound, m/s
$B_{\bar{W}}$	=	bias error of average wave-speed measurement
D	=	shock-tube inside diameter
e_{hys}	=	elemental uncertainty from sensor hysteresis
e_{lin}	=	elemental uncertainty from nonlinearity in sensor response
e_{rep}	=	elemental uncertainty from sensor measurement reproducibility
e_{sen}	=	elemental uncertainty from sensor sensititivity
e_{tot}	=	total elemental uncertainty
e_z,	=	elemental uncertainty from sensor drift from zero point
M	=	Mach number
$P_{\bar{W}}$	=	precision error of average wave-speed measurement
p	=	pressure, atm
p_c	=	critical pressure, atm
p_1	=	low-pressure initial state, atm
p_3	=	state at tail of expansion fan, atm
p_4	=	high-pressure initial state, atm
Re_D	=	Reynolds number based on tube diameter
s	=	specific entropy, J/kg · K
T	=	temperature, °C
t	=	time, s
t_{h}	=	time of passage of rarefaction wave head at sensor 1, s
$t_{\text{t}}, t'_{\text{t}}$	=	simulated and measured time of passage of rarefaction wave tail at sensor 1, s
t_0	=	initial time at diaphragm rupture, s
$U_{\bar{W}}$	=	total error of average wave-speed measurement
v	=	specific volume, m^3/kg
v_c	=	critical specific volume, m^3/kg
$\bar{W}$	=	average wave speed, m/s
x, y, z	=	space coordinates
x_{dia}	=	axial location for diaphragm and high-pressure side of piecewise linear pressure distribution in simulation coordinates, m
x_{S1}	=	axial location of sensor 1 in simulation coordinates, m
x'	=	axial location for low-pressure side of piecewise linear pressure distribution in simulation coordinates, m
Γ	=	fundamental derivative of gasdynamics
ΔL	=	dynamic pressure sensor separation, m
Δp_{inc}	=	pressure change across incident rarefaction wave, atm
Δp_{sec}	=	pressure across reflected secondary rarefaction wave, atm
Δt	=	wave propagation time, s
Δt_{open}	=	diaphragm opening time, s

Presented as Paper 2001-2747 at the AIAA 35th Thermophysics Conference, Anaheim, CA, 11–14 June 2001; received 12 August 2002; revision received 11 February 2003; accepted for publication 11 February 2003.

*Member, Technical Staff, The Aerospace Corporation, P. O. Box 92957, M4-967. Member AIAA.
†Research Assistant, Dipartimento di Ingegneria Aerospaziale, Campus Bovisa Sud, via La Masa 34.
‡Associate Professor, Department of Aerospace Engineering Sciences, CB 429 UCB. Senior Member AIAA.

Introduction

DENSE gasdynamics refers to the behavior of a single-phase vapor near the saturated vapor portion of the coexistence curve, adjacent to the thermodynamic critical point. The nonlinear supersonic wave field is governed by the fundamental derivative of gasdynamics, which is written in nondimensional form as

$$\Gamma = 1 + \frac{\rho}{a}\left.\frac{\partial a}{\partial v}\right|_s \tag{1}$$

The sign of Γ determines the type of wave field nonlinearity. The familiar positive nonlinearity of classical gasdynamics, for example, dynamics of an ideal gas, is associated with positive Γ values.

Cramer[1] refers to the class of fluids that exhibit negative nonlinearity, with $\Gamma < 0$, as Bethe–Zel'dovich–Thompson (BZT) fluids. The $\Gamma < 0$ condition corresponds to the reversal of curvature of the isentropes in the p–v plane with respect to the well-known polytropic ideal gas behavior. Contrary to an ideal gas, a consequence of negative nonlinearity is that the speed of sound increases during an isentropic expansion. (See, for example, Cramer[1] for a comprehensive discussion of Γ and dense gasdynamics.)

Negative nonlinearity results in a reversal of the classical supersonic wave field, where compression shock waves and rarefaction fans are replaced by compression fans and rarefaction shock waves. In regions of mixed (positive and negative) nonlinearity, composite waves consisting of a mix of classical and nonclassical waves might exist. The most significant of the nonclassical phenomena is the rarefaction shock wave (RSW). Duhem[2] first theorized the existence of the RSW and argued (incorrectly) that a single-phase RSW violates the second law of thermodynamics. In 1942, Bethe[3] found the necessary conditions for a van der Waals fluid to exhibit nonclassical behavior in the single-phase vapor region. Thompson[4] later showed that an RSW is possible for a fluid with negative Γ. Thompson and Lambrakis[5] and Cramer[6] listed several commercial fluids that might exhibit nonclassical behavior.

Numerous analytical[1–7] and computational[8–13] studies have provided insight into dense gas phenomena. This includes the RSW, compression fans, sonic shocks,[14,15] and shock splitting[1,16,17] for a pure single-phase gas. Experiments have verified nonclassical behavior in two-phase systems.[18,19] Complementary experimental studies of nonclassical phenomena in a single-phase vapor, however, remain undone. Borisov et al.[20] claimed to demonstrate a single-phase RSW in a shock-tube experiment using trifluorochloromethane (commercial name Freon-13 or F-13). The experiment recorded an expansion wave with a width of approximately 3 cm propagating with little change in profile. Borisov et al.[20] and Kutateladze et al.[21] assert that this wave was an RSW. Fergason et al.[22] challenged this assertion, based on two points. First, F-13 is not a retrograde fluid, a necessary property for a BZT fluid, and, secondly, $\Gamma \to +\infty$ as the critical point is approached. The Borisov et al.[20] F-13 experiment was computationally modeled by Fergason et al.[22] using the Martin–Hou equation of state.[23] The result, reproduced in Fig. 1, shows a rarefaction fan (RF) below both the coexistence and spinodal curves when plotted in the p–v plane. The RF is separated from the compression shock wave (CSW) by the v jump through the contact surface (CS). Although the simulation is not expected to be highly accurate near the critical point and in the two-phase region, the qualitative results suggest that a RSW in F-13, even with metastable intermediate states, is not possible. Others,[14,24] and even Kutateladze et al.,[21] questioned the interpretation of the Borisov et al.[20] experiment and offered alternative explanations related to the influence of the thermodynamic critical point.

The uncertainty of the experiment with F-13 provides motivation for the planned dense gas experiments. We attempt to avoid ambiguity by choosing a BZT fluid and initial states sufficiently removed from the critical point to avoid its nonanalytic influence.

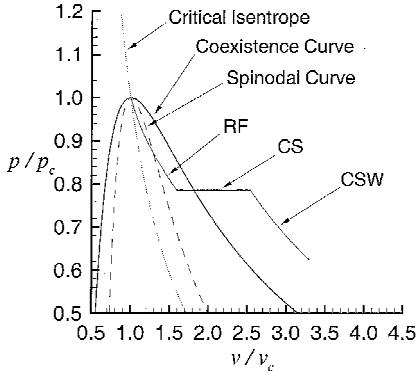

Fig. 1 Coexistence curve, critical isentrope, spinodal curve, and simulated p–v states for F-13 shock-tube simulation.[22]

Fergason et al.[22] presented an algorithm to identify appropriate initial conditions for a given BZT fluid. This algorithm was used in the design and construction of the dense gas shock tube. The present work summarizes the construction and subsequent validation of the shock tube operating in conditions predicted to produce nonclassical behavior in BZT fluids.

The next section outlines the features of the experimental apparatus. Specific design parameters are discussed along with relevant schematics. In the following sections, results of experimental validation trials using nitrogen (N_2) are discussed. A measurement uncertainty analysis is also presented. Finally, results from numerical experiments are compared to actual experimental results to investigate the influence of the diaphragm bursting dynamics.

Experimental Apparatus

The shock tube is designed to verify the existence of nonclassical phenomena associated with single-phase, dense gasdynamics. Temperature and pressure are controlled to set the initial conditions. Figure 2 shows the location of a particular set of initial conditions computed using the algorithm of Fergason et al.[22] for perfluoroperhydrofluorene ($C_{13}F_{22}$, commercial name PP10), which will be the first BZT fluid tested. Figure 2 was created using the Martin–Hou equation of state and shows the saturated vapor portion of the coexistence curve with the $\Gamma < 0$ region enclosed between the coexistence curve and the $\Gamma = 0$ contour. The standard shock-tube numbering scheme[10] is used to designate the initial low-pressure state 1 and the high-pressure state 4. The region of initial states shown in Fig. 2 is typical of that for the BZT fluids considered. The range of available states offers little margin for uncertainty in either the fluid pressure or temperature with readily available sensors.

The dense gas shock tube, shown schematically in Fig. 3, is designed to use a single fluid in the driver and driven sections. This avoids a complex fluid separation system and simplifies the analysis. Sustaining an initial temperature differential across the diaphragm was not considered. The main tube is made from Type 304, 4-in. Schedule 80 stainless steel tubing, with an outside diameter of 11.43 cm (4.500 in.) and an inside diameter of $D = 9.718$ cm (3.826 in.). The 4.88-m (16.0-ft) long tube is completely contained within the heating elements of the tube furnace. The diaphragm is

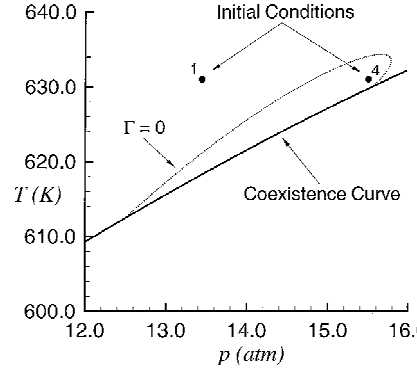

Fig. 2 Candidate initial conditions in the T–p plane for PP10 using the Martin–Hou[23] equation of state and assuming nonpolytropic behavior in the dilute gas limit.

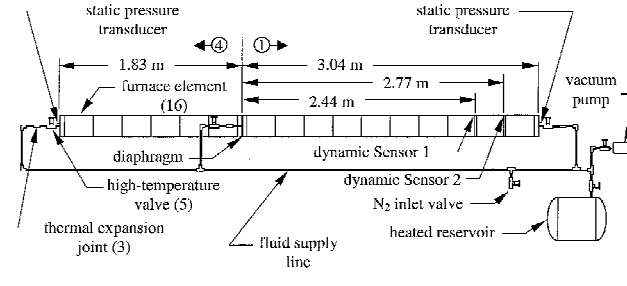

Fig. 3 Shock-tube schematic.

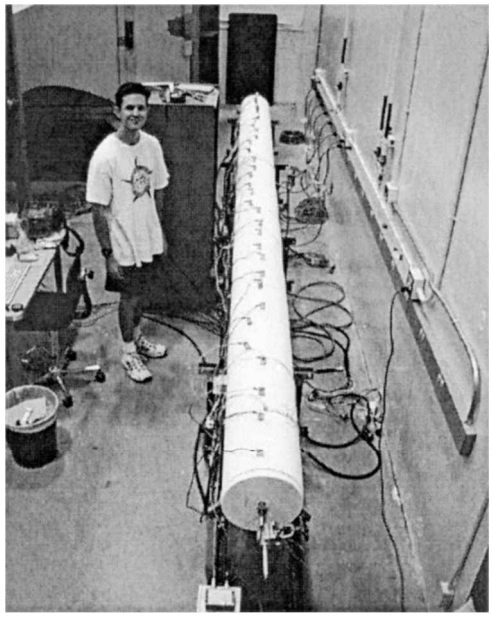

Fig. 4 Photograph of shock tube.

offset 3.04 m (10 ft) from the end of the tube that contains the dynamic transducers. The labels 1 and 4 in Fig. 3 indicate the low- and high-pressure sides of the shock tube initially separated by the diaphragm. The two dynamic pressure transducers are located at $x/D = 25.1$ and 28.5 from the diaphragm at distances of 2.44 m (8.00 ft) and 2.77 m (9.08 ft), respectively. The locations of high-temperature valves, thermal expansion joints, and vapor distribution equipment are also shown. Figure 4 is a photograph of the shock tube with the first author. The furnace heater segments can be distinguished in the photograph.

Temperature Control Subsystem

Because the temperature interval to observe nonclassical gasdynamics is the most restrictive aspect of these experiments (cf. Fig. 2), adequate precision and accuracy for the temperature control system is a fundamental requirement. The temperature control system consists of 16 individual control loops administered by a CPU. Each individual loop comprises a proportional–integral–differential control algorithm with a thermocouple as sensor input and an 1800-W resistance heater as negative output. By division of the control task among many different control elements over the length of the tube, the accuracy of the temperature control is comparable to the accuracy of each individual control element. This is possible because the system temperature response time is considerably slower than the administration of the algorithm for the 16 control loops.

Temperature measurement at elevated values is made accurate and precise with the use of the F150/B550 high-accuracy calibration system from ASL, Inc. Thermocouples and resistance temperature detectors operate reliably above 200°C with approximately the same amount of error. The use of National Institute of Standards and Technology calibrations gives a listed error value of ±2°C for both sensor types. Because this temperature accuracy was unacceptable for this experiment, a different calibration was implemented. With a manufacturer listing of ±0.01°C, the temperature was measured within the desired range for each individual element of the control system.

When the shock tube is fully operational, the reservoir shown in Fig. 3 will be filled with a BZT fluid (PP10 initially), then heated to generate the vapor to fill the tube. The reservoir was not used for the present N_2 tests. For each run, the shock tube was brought to the initial set-point temperature before the N_2 was introduced. Figure 5 shows a typical heating history of the 16 furnace elements as they approached a set-point temperature of 300°C. Although the individual curves are not labeled to correspond to Fig. 3, the elements near the center of the heater array approached the set-point temperature

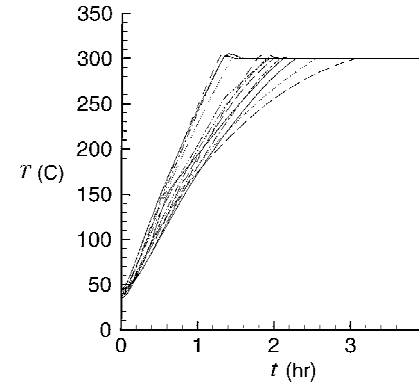

Fig. 5 Temperature history for 16 furnace sections with a 300°C set-point temperature.

more quickly then those near the ends. Room temperature N_2 was introduced into both sides of the shock tube through the N_2 inlet supply valve. The N_2 was evacuated twice to purge the system of air before the final pressurization. The system was then allowed to reequilibrate to the set-point temperature before bleeding the N_2 to the required initial pressure differential. Leakage was not a problem for these initial tests; however, future tests will quantify the leak rate before the dense gas experiments begin.

Data Acquisition Subsystem

Data acquisition was focused on two sets of measurements, the initial static pressure and temperature and the dynamic pressure. Although the high- and low-pressure states can be swapped from one end to the other, the focus of experiments was the propagation of the rarefaction wave into the high-pressure state 4. The requirements on temperature control and high-temperature sealing precluded an optical window in the present design.

For the N_2 experiments, the rarefaction wave front moves at the state-4 speed of sound, typically about 500 m/s. Based on this speed, Re_D is on the order of 1×10^6, thus, a turbulent boundary layer is expected. Because the boundary layer grows from zero thickness with the passage of the head of the rarefaction wave, it is expected to have a negligible effect on the pressure measurements of the incident wave. Fergason and Argrow[25] presented simulation results for boundary-layer growth behind a RSW in a BZT fluid, including a discussion of the resulting negative displacement thickness.

The Kistler Instrument Corporation manufactured the piezoelectric dynamic pressure transducers and the piezoresistive static pressure transducers. The dynamic transducers are mounted in the wall of the stainless steel main tube. These transducers were chosen for their ability to withstand the sustained high temperatures without sacrificing precision or accuracy. The casing surrounding the electronics of these transducers is water cooled. The initial pressure conditions are measured with static pressure transducers mounted on stalks (small-diameter stainless tubes) at each end of the shock tube. The stalks allow the static transducers to be placed outside the high-temperature environment inside the furnace. In addition, a cooling adaptor is mounted to ensure that the static electronics stay within operating tolerances. The stalk design is also intended to remove thermal gradients introduced to the fluid by the cooling adaptors. The static sensor stalks are mounted in the flange caps at each end of the tube. A bore in the end cap insulation allows the sensor cabling and cooling lines to be attached without direct exposure to the high-temperature interior.

The input side of the control algorithm uses high-temperature type-K thermocouple wire to measure the initial fluid temperature. Thermocouples are used because they provide adequate accuracy and durability and are easily fabricated. Two thermocouples are inserted into each end cap of the tube to confirm the internal initial temperature. Thermocouples are placed on the tube exterior, spaced 30.4 cm (12.0 in.) apart, beneath each of the furnace segments. Each thermocouple provides a wall temperature measurement for the control algorithm.

Diaphragm Preparation

The diaphragm is a 0.1-mm (0.004-in.) thick copper sheet with a cross-patterned score for a rapid, even burst. A double diaphragm system was attempted initially, but was abandoned due to a lack of repeatability from the limited selection of materials investigated. A mechanical bursting mechanism was also considered, but not pursued. To initiate the experiment, the entire tube is brought to the high-pressure state. Then the pressure is slowly lowered on the low-pressure side until the diaphragm bursts within the range of allowable initial conditions.

Results

Experimental trials using nitrogen were completed to investigate the accuracy and repeatability of the apparatus with conditions similar to those expected to produce a nonclassical wave field in a BZT fluid. Data collected from the dynamic sensors are in the form of a voltage measured in evenly spaced time increments. The nitrogen wave field is composed of a classical RF propagating into the high-pressure side (state 4) and a CSW, followed by a CS, propagating into the low-pressure side (state 1). Between the rarefaction wave and the compression shock, the pressure is p_3.

The results of these trials are summarized in the following section. The initial conditions were also input into a numerical simulation for comparison with the experiments. These simulation results are also discussed.

Nitrogen Tests

The data presented in Figs. 6–8 are for case 1 listed in Table 1; these data are representative of each of the four nitrogen trials.

Table 1 Initial conditions and sampling rates

Case	p_1, atm	p_4, atm	T, °C	Sample, Hz
1	4.250	4.824	350.0	44,642
2	3.980	4.736	350.0	52,083
3	4.237	4.825	350.0	52,083
4	4.539	5.219	350.0	104,166

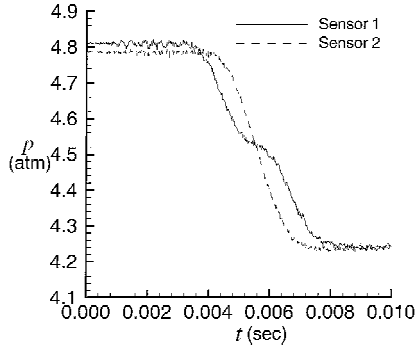

Fig. 6 Dynamic sensor pressure history for case 1.

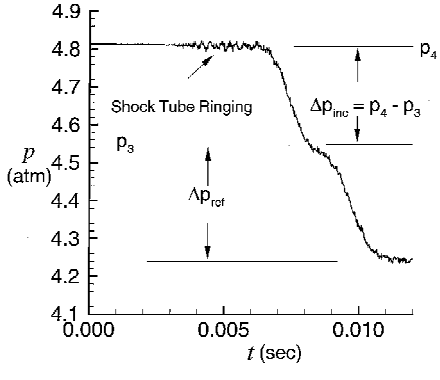

Fig. 7 Interpretation of pressure signal.

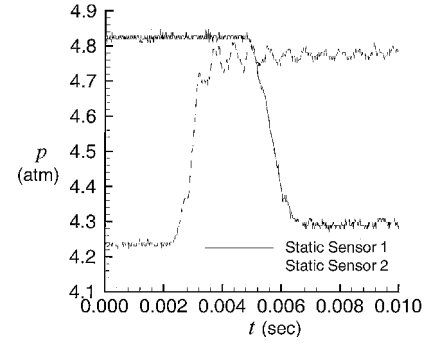

Fig. 8 Pressure history from static sensors for case 1.

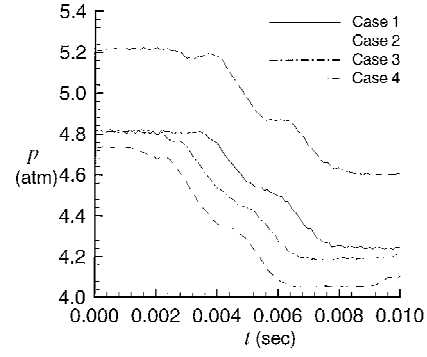

Fig. 9 Pressure history from dynamic sensor 1 for initial conditions in Table 1.

Figure 6 shows the incident expansion wave at the two wall-mounted dynamic pressure sensors, and Fig. 7 helps to interpret the data in Fig. 6. The incident wave front recorded by the static pressure sensors is shown in Fig. 8. Note that static sensor 2 recorded the CSW signature. The repeatability of the bursting process was established as shown in Fig. 9 for the four separate experimental trials, with slightly varying initial conditions. Because the focus of the study is on incident waves, Figs. 6–9 show only the initial sensor contact with a wave. Further time evolution, after multiple end-wall reflections, was measured, but is not shown.

In Fig. 6, sensor 1 is the dynamic pressure sensor closest to the diaphragm, and sensor 2 is the dynamic pressure sensor closest to the end-wall. At first the expansion wave appears more complicated than expected. Sensor 1 shows evidence of a "stepped" expansion wave, not evident at sensor 2. The upper part of the stepped wave spans a pressure decrease approximately equal to the Δp_{inc} predicted by the exact solution of the ideal gas Riemann problem for N_2. The stepped appearance is not evident in the sensor 2 profile, and the magnitude of the pressure decrease is about twice that predicted from the Riemann problem. However, the end of the expansion shown in Fig. 6 ($t \approx 0.008$ s) occurs for sensor 2 before sensor 1, suggesting that a wave traveled in the opposite direction to the incident expansion fan. This observation is further supported in Fig. 8 by the detection of a pressure decrease at $t \approx 0.005$ s (before termination of the total pressure decrease in Fig. 6) by static sensor 1.

It is clear in Fig. 6 that the expansion wave measured at sensor 1 was a combination of the incident expansion fan and the end-wall reflection propagating in the opposite direction. The smoothly varying expansion of double magnitude suggests that sensor 2 was in the nonsimple wave region of the reflection, so that it did not distinguish between the incident and reflected waves.

The average wave speed is calculated from the difference in time of arrival of the head of the pressure wave at each dynamic sensor. Because the sensor spacing is accurately known, the average wave speed is simply

$$\bar{W} = \Delta L / \Delta t \tag{2}$$

Because the wave travel time is inferred from the dynamic pressure measurement, the dynamic sensor error and the sampling rate directly affect the time measurement.

Table 2 Theoretical vs measured shock tube conditions

	p_3, atm		$\bar{W}$, m/s	
Case	Theory	Experiment	Theory	Experiment
1	4.519	4.525 ± 0.016	507.0	503.6 ± 93.2
2	4.339	4.338 ± 0.016	507.0	490.7 ± 69.2
3	4.520	4.442 ± 0.016	507.0	545.5 ± 76.7
4	4.865	4.866 ± 0.016	507.0	525.4 ± 43.5

Table 3 Elemental uncertainties for dynamic and static pressure sensors

Elemental uncertainty	Dynamic		Static	
	% FSO[a]	atm	% FSO[a]	atm
e_{hys}	≤0.5	≤0.004	≤0.1	≤0.020
e_{lin}	±0.1	±0.001	±0.3	±0.060
e_{rep}	±0.5	±0.004	≤0.1	≤0.020
e_{sen}	±0.5	±0.004	≤0.2	≤0.040
e_{zl}	±6.7	±0.050	≤0.1	≤0.020
e_{zs}	±0.5	±0.004	≤0.1	≤0.020
e_{totl}	±6.8	±0.050	±0.4	≤0.080
e_{tots}	±2.1	±0.016	±0.4	≤0.080

[a]Full scale output.

Table 2 compares the incident experimental expansion wave with one-dimensional Euler predictions using the initial conditions in Table 1. The p_3 values following the incident expansion wave match predicted values to within 2% for all cases, and the computed $\bar{W}$ value is within the uncertainty of the measured $\bar{W}$ values.

Uncertainty Analysis

The simplicity of the shock-tube system leads to simple evaluations for the individual and overall system uncertainties. The experimental uncertainty is confined to that in the pressure and temperature measurements, which propagate to any associated variables calculated from those measurements.

The elemental uncertainty for the pressure sensors is computed from

$$e_{tot} = \sqrt{e_{hys}^2 + e_{lin}^2 + e_{rep}^2 + e_{sen}^2 + e_z^2} \tag{3}$$

See, for example, Figliola and Beasley[26] or Holman.[27] Table 3 lists the individual sources with the total sensor uncertainty listed in the manufacturer's specifications.[28,29] Two distinct values of the zero-drift uncertainty (subscripted s for short time and l for long time) are listed in Table 3. The zero-drift uncertainty results from the drift of the sensor ground (reference pressure) over time. Because a period of seconds elapses between the sensor initiation and the recording of the data of interest, a small drift is possible in the reference pressures of the individual sensors, represented by the long time uncertainty. The short time zero-drift uncertainty represents the effect of the ground drift of the individual channels over the course of a typical measurement, for example, 0.001 s. These values represent the uncertainty in any pressure measurement for the apparatus and are, thus, used as error-bar magnitudes for any physical representation involving pressure data.

The elemental uncertainty for any measurement system can be estimated using the preceding procedure. However, estimating the temperature elemental uncertainty becomes much simpler with end-to-end calibration. By calibration of the entire temperature measurement system, the individual sources are replaced by the uncertainty of the calibration technique. In this case, the temperature calibration uncertainty is listed as 0.01°C. Because the temperature resolution of the thermocouple is 0.1°C, this value becomes the temperature elemental uncertainty and is used for the error-bar magnitude in all temperature data.

The inherent uncertainty in the wave speed is calculated using standard error propagation techniques.[26,27] Bias errors $B_{\bar{W}}$ and precision errors $P_{\bar{W}}$ are estimated for the average wave speed from the uncertainty in the sensor displacement, whereas the wave arrival time is based on the sensor's ability to detect temporal pressure changes. The data sampling rate and the dynamic sensor uncertainty are factors that influence the wave arrival measurement. The total error

$$U_{\bar{W}} = \sqrt{B_{\bar{W}}^2 + P_{\bar{W}}^2}$$

for the average wave speed is also presented in Table 4.

Table 4 Uncertainties for experimental average wave speeds

Case	$B_{\bar{W}}$, m/s	$P_{\bar{W}}$, m/s	$U_{\bar{W}}$, m/s
1	±76.7	±0.9	±76.7
2	±69.2	±0.8	±69.2
3	±93.2	±0.8	±93.2
4	±43.5	±0.9	±43.5

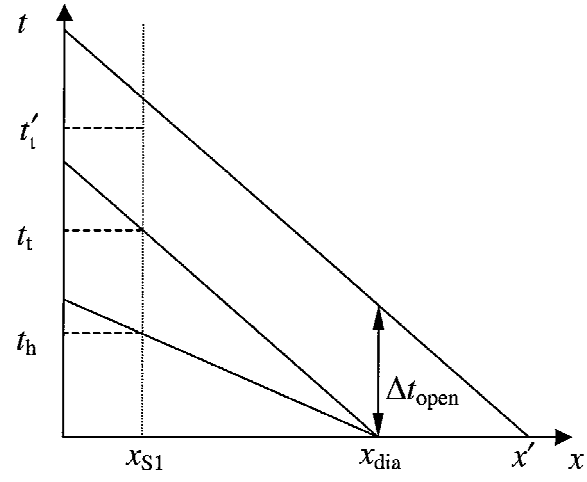

Fig. 10 Diaphragm opening time in x–t plane.

Diaphragm Bursting Process

The influence of the diaphragm bursting process on the measurements is now discussed. Specifically, we examine the effects of the bursting process on the measured expansion wave pressure profiles. First, the theory of characteristics is used to estimate the diaphragm breaking time. This is essentially the time it takes for state 3 to be established at the tail of the expansion fan. Then numerical simulations are presented to investigate the effects on the wave field evolution from incomplete diaphragm petaling.

Diaphragm Opening Time

The experimental results for case 1 in Table 1 give an elapsed time between the detection of the head of the incident rarefaction wave and its tail, which is greater (1.59×10^{-3} s) than predicted by theory (2.78×10^{-4} s). As a consequence, the p vs t slope of the measured incident wave (cf. Fig. 6) is significantly lower than predicted. This discrepancy is believed to depend partly on the finite diaphragm opening time. The influence of nonideal behavior of the diaphragm on shock-tube flows is addressed extensively in the literature,[30–34] although most authors focused their analysis on the compression side of the tube. For a high-pressure ratio p_4/p_1 apparatus, the finite opening time may result in shock wave acceleration along the tube axis and also to higher shock speeds with respect to ideal one-dimensional theory.[31,33,34]

By the assumption of a linear time dependence of the pressure at the diaphragm location x_{dia} (i.e., a linear decrease from the value p_4 at time t_0 to the final value p_1 at time $t_0 + \Delta t_{open}$), it is possible to estimate Δt_{open} from the theory of characteristics (Fig. 10). This is obtained from the exact solution of the Riemann problem, that is, for an instantaneous diaphragm burst. The characteristic lines drawn through t_t and t_t' are parallel because they correspond to the same

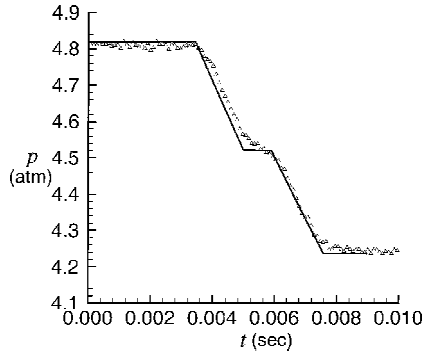

Fig. 11 Experiment and computational pressure history, dynamic sensor 1, case 1.

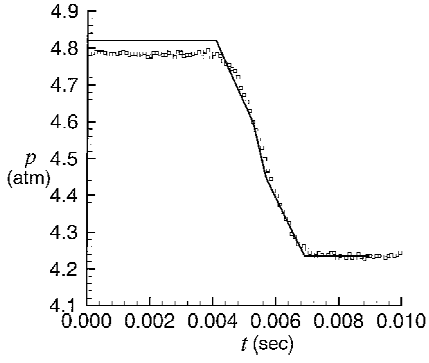

Fig. 12 Experiment and computational pressure history, dynamic sensor 2, case 1.

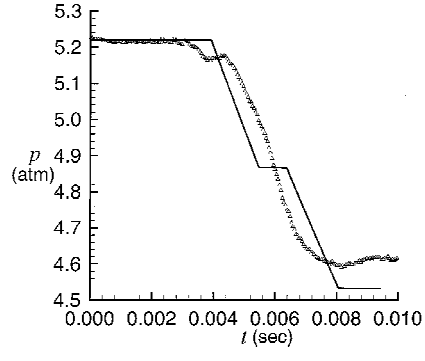

Fig. 13 Experiment and computational pressure history, dynamic sensor 1, case 4.

gas dynamic state 3. Thus, the diaphragm opening time is immediately obtained as $t_t' - t_t$, or 1.31×10^{-3} s for case 1. This opening time is consistent with the cited references. For example, White[31] measured $\Delta t_{open} = 6 \times 10^{-4}$ s for 0.406-mm thick type 302 stainless steel diaphragms, with $p_4/p_1 > 1000$ (for the present apparatus $p_4/p_1 \cong 1.14$). Note that the measured time t_t' is also evidently influenced by the incomplete petaling, discussed in the next section. The primary effect is a decrease in the slope of the p–x plot of the expansion profile (discussed in the next section), thus resulting in a corresponding increase in t_t'.

Numerical simulations are now presented to support the present explanation. In Figs. 11 and 12, the numerical results for case 1 of Table 1 are compared with the corresponding experimental values. A linear pressure distribution from time t_0 to $t_0 + \Delta t_{open}$ can be obtained by supplementing the numerical simulation with a piecewise linear (in space) initial condition at time t_0, in which the pressure varies from p_4 at x_{dia} to p_1 at x', as shown in Fig. 10, to avoid unnecessary complications related to time-dependent boundary conditions.

The estimated diaphragm opening time is verified by consideration of case 4 of Table 1, as shown in Figs. 13 and 14. In fact,

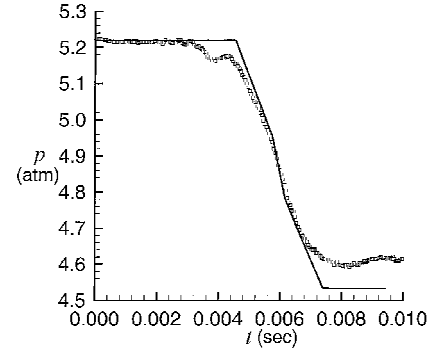

Fig. 14 Experiment and computational pressure history, dynamic sensor 2, case 4.

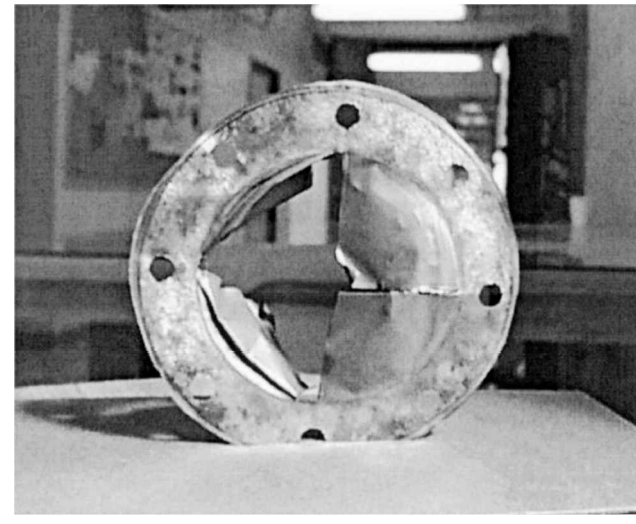

Fig. 15 Typical burst diaphragm.

the ratio p_4/p_1 being about the same as in case 1, the diaphragm opening time should not vary significantly. Numerical simulations agree with the observed pressure profile trends, thus confirming the present estimate. In both cases, dynamic pressure sensor 2 lies inside the nonsimple region of wave reflection at the end wall.

It is worth addressing the diaphragm tearing process and its influence on the wave profile. As pointed out by Rothkopf and Low,[32] copper or brass diaphragms are characterized by a longer tearing time with respect to less ductile materials such as aluminum. The tearing process can take as much as 50% of the total bursting time. Moreover, ductile materials have been found to present asymmetric petaling, a behavior that is enhanced in the present case by the circular shape of the diaphragm.[32] The strong oscillation in the pressure profile of Fig. 13, which is located immediately ahead of the main rarefaction wave and that is more intense than the background shock-tube ringing, appears to be related to the asymmetric petaling of the diaphragm. A similar, though weaker, disturbance is also visible in Fig. 11.

Partial Burst of the Diaphragm

Posttest examination of the diaphragms indicates nonuniform petaling. In each case, the diaphragm burst correctly along the prescribed score, yet only two adjacent petals, of the four, appear to have been forced completely open. An example of a partially burst diaphragm is shown in Fig. 15, where the partial petaling is evident. This obstacle to the main flow may create a multidimensional secondary flow not adequately modeled by the one-dimensional Riemann problem. Three-dimensional Euler simulations are presented next, to examine the influence of the asymmetric burst on the measurements.

The high-resolution approach proposed by Guardone and Quartapelle,[35] which combines the node-pair representation[36] of the

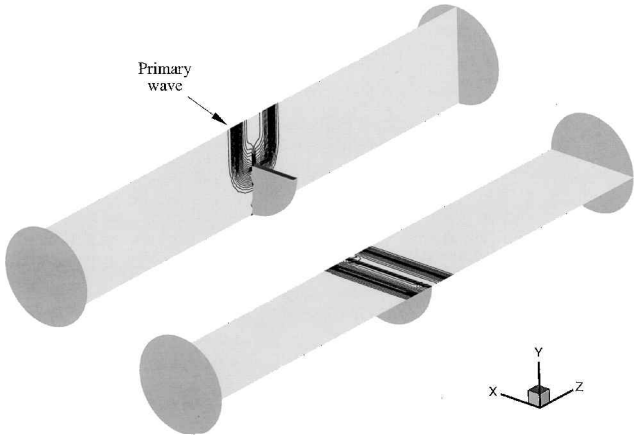

Fig. 16 Three-dimensional simulation of partial diaphragm burst, $t = 0.048 \times 10^{-3}$ s, isoline difference 6×10^{-3} atm.

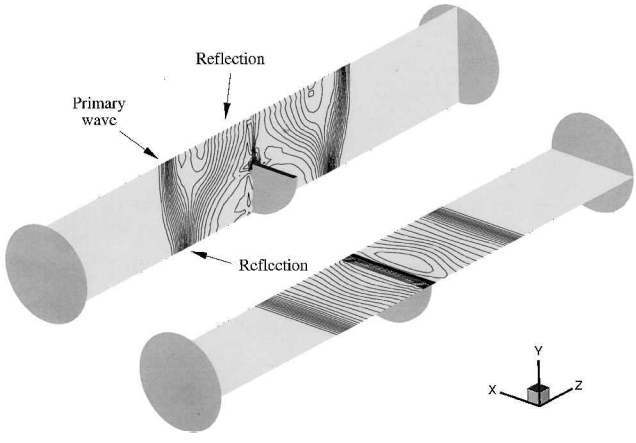

Fig. 17 Three-dimensional simulation with partial diaphragm burst, $t = 0.24 \times 10^{-3}$ s, isolines at 12×10^{-3} atm.

Galerkin and Taylor–Galerkin schemes with the upwind scheme of Roe[37] for polytropic ideal gases, is employed in the computations. For a detailed description of the method, the reader is referred to Selmin[36] and to Selmin and Formaggia.[38]

The shock-tube geometry is discretized by means of an unstructured grid of 170,829 prismatic elements with triangular basis (96,192 nodes). Note that, for the three-dimensional simulation plots, the shock-tube centerline is designated as the z axis. In the z direction, the grid is evenly spaced to obtain a resolution of 10 mm (501 nodes). In each x–y cross section, the grid is made of 342 triangles, to obtain an average distance between nodes of about 8 mm. The surface grid of the diaphragm is a hybrid of 342 triangles (diaphragm sides) and 13 quadrilaterals (diaphragm top). With the grid spacing being uniform in the z direction, the diaphragm thickness is 10 mm.

Figures 16 and 17 show the pressure contours at times $t = 0.048 \times 10^{-3}$ s and 0.24×10^{-3} s in the $x = 0$ and $y = 0$ planes, for case 1 of Table 1; the spacing of the pressure isolines is 12×10^{-3} atm. The vertical section of the diaphragm induces a curved expansion front that moves into the high-pressure test section. On contacting the lower wall, the oblique expansion reflects to produce the series of expansions seen in the pressure contours of Fig. 17. The compression shock undergoes a similar reflection as it moves into the low-pressure side of the shock tube. The primary rarefaction wave has a lower intensity than the one resulting from a full burst of the diaphragm. The preceeding agrees with the theory of cylindrical waves, which predicts a reduction in the wave intensity that is proportional to the inverse of the distance from its center. Because of the initial curvature of the waves, the primary and reflected waves eventually coalesce into a single wave orthogonal to the shock-tube axis because the portion of the wave that is normal to the shock tube walls moves at a lower velocity (relative to the wall) than the curved part. Therefore, a single rarefaction wave, normal to the shock tube axis, is obtained near the end wall, exactly as in the case of a completely burst diaphragm.

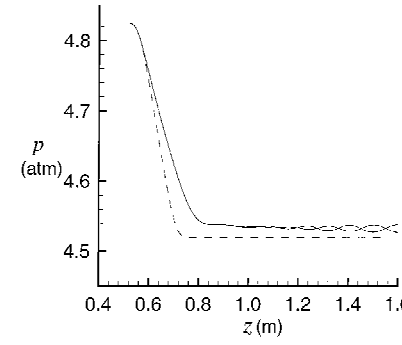

Fig. 18 Three-dimensional simulation with partial diaphragm burst near dynamic sensor 1.

The pressure transducers are located near the end wall where the single rarefaction wave is completely formed (cf. Fig. 18). However, the slope of the rarefaction wave differs from the one resulting from a complete burst because it is generated by a reflection process, rather than an initial discontinuity as in the one-dimensional Riemann problem. Moreover, the overall pressure difference across the rarefaction wave is smaller than the expected value. This discrepancy can be explained by consideration of the primary wave as it first leaves the diaphragm. The rarefaction wave sets the fluid into motion toward the diaphragm; as the fluid encounters the diaphragm surface, a compression wave starts from the diaphragm location toward the primary wave. This compression wave weakens the primary and the reflected secondary rarefaction waves, thus resulting in the pressure jump reduction that is observed in Fig. 18. The reduction of the pressure difference across the rarefaction wave is between 0.01 and 0.02 atm, and, therefore, the presence of this effect went unnoticed in the preliminary tests because of the lack of pressure sensor resolution. (Sensor resolution for the nitrogen test cases is ± 0.016 atm.)

Conclusions

A shock tube designed to explore the dynamics of dense gases, particularly the nonclassical dynamics of BZT fluids, has been constructed and tested with N_2. The primary goal of these experiments was to validate the design for use in the region of pressures and temperatures expected to produce the nonclassical behavior of a BZT fluid. The entire tube was heated to a uniform initial temperature of 350°C. Heating is provided by 16 tube-furnace segments for precise temperature control over the entire length of the tube. A single copper diaphragm is used to initiate each experimental trial. The diaphragms consistently burst with acceptable repeatability; however, petaling was not complete.

The results of each experimental trial are compared to the ideal gas Riemann problem for validation of the bursting process and data acquisition. The incident expansion wave matched the theoretical magnitude to within 2%. The average wave speed measured for each trial was found to match the theoretical value to within 7% and within the calculated uncertainty.

The influence of the finite diaphragm opening time is estimated with a one-dimensional model employing a simple linear profile for the initial transient pressure response. The diaphragm opening time is estimated as 1.31×10^{-3} s, and it significantly affects the profile of the propagating RFs.

The experiment was simulated with a three-dimensional Euler computation to examine the effect of an obstacle on incident wave propagation. The bursting process was modeled with a partial diaphragm break. This was based on examination of diaphragms after experimental trials. Simulations show that a partial diaphragm burst did not significantly affect classical expansion fan formation.

Acknowledgment

This research was supported, in part, by the National Science Foundation under Grant CTS-1531173.

References

[1]Cramer, M. S., "Nonclassical Dynamics of Classical Gases," *Nonlinear Waves in Real Fluids*, edited by A. Kluwick, Springer-Verlag, Berlin, 1991, pp. 91–145.

[2]Duhem, P., "Sur la Propagation des Ondes de Choc au Sein des Fluides," *Zeitschrift für Physikalische Chemie*, Vol. 69, No. 2, 1909, pp. 169–186.

[3]Bethe, H. A., "The Theory of Shock Waves for an Arbitrary Equation of State," Technical Rept. 545, Office of Scientific Research and Development, Washington, DC, 1942.

[4]Thompson, P. A., "A Fundamental Derivative in Gas Dynamics," *Physics of Fluids*, Vol. 14, No. 9, 1971, pp. 1843–1849.

[5]Thompson, P. A., and Lambrakis, K., "Negative Shock Waves," *Journal of Fluid Mechanics*, Vol. 60, Pt. 1, 1973, pp. 187–208.

[6]Cramer, M. S., "Negative Nonlinearity in Selected Fluorocarbons," *Physics of Fluids*, Vol. 1, No. 11, 1989, pp. 1894–1897.

[7]Menikoff, R., and Plohr, B. J., "The Riemann Problem for Fluid Flow of Real Materials," *Reviews of Modern Physics*, Vol. 61, No. 1, 1989, pp. 75–129.

[8]Müller, S., and Voβ, A., "An Iterative Riemann Solver for the Euler Equations and Nonconvex Equation of State," Institut für Geometrie und Praktische Mathematik Rept. 168, Rheinisch-Westfälische Technische Hochschule–Aachen, Germany 1999.

[9]Cramer, M. S., and Tarkenton, G. M., "Transonic Flows of Bethe–Zel'dovich–Thompson Fluids," *Journal of Fluid Mechanics*, Vol. 240, 1992, pp. 197–228.

[10]Argrow, B. M., "Computational Analysis of Dense Gas Shock Tube Flow," *Shock Waves*, Vol. 6, No. 4, 1996, pp. 241–248.

[11]Brown, B. P., and Argrow, B. M., "Two-Dimensional Shock Tube Flows for Dense Gases," *Journal of Fluid Mechanics*, Vol. 349, 1997, pp. 95–115.

[12]Bates, J. W., and Montgomery, D. C., "Some Numerical Studies of Exotic Shock Wave Behavior," *Physics of Fluids*, Vol. 11, No. 2, 1999, pp. 462–475.

[13]Guardone, A., and Vigevano, L., "Roe Linearization for the van der Waals Gas," *Journal of Computational Physics*, Vol. 175, No. 1, 2002, pp. 50–78.

[14]Cramer, M. S., and Sen, R., "Shock Formation in Fluids Having Embedded Regions of Negative Nonlinearity," *Physics of Fluids*, Vol. 29, No. 7, 1986, pp. 2181–2191.

[15]Cramer, M. S., and Sen, R., "Exact Solutions for Sonic Shocks in van der Waals Gases," *Physics of Fluids*, Vol. 30, No. 2, 1987, pp. 377–385.

[16]Cramer, M. S., "Shock Splitting in Single-Phase Gases," *Journal of Fluid Mechanics*, Vol. 199, 1989, pp. 281–296.

[17]Cramer, M. S., and Sen, R., "Mixed Nonlinearity and Double Shocks in Superfluid Helium," *Journal of Fluid Mechanics*, Vol. 221, 1990, pp. 233–261.

[18]Thompson, P. A., and Kim, Y., "Direct Observation of Shock Splitting in a Vapor–Liquid System," *Physics of Fluids*, Vol. 26, No. 11, 1983, pp. 3211–3215.

[19]Thompson, P. A., Carofano, G. A., and Kim, Y., "Shock Waves and Phase Changes in a Large Heat Capacity Fluid Emerging from a Tube," *Journal of Fluid Mechanics*, Vol. 166, 1986, pp. 57–96.

[20]Borisov, A. A., Borisov, A. L., Kutateladze, S. S., and Nakoryakov, V. E., "Rarefaction Shock Wave Near the Thermodynamic Critical Point," *Journal of Fluid Mechanics*, Vol. 126, 1983, pp. 59–73.

[21]Kutateladze, S. S., Nakoryakov, V. E., and Borisov, A. A., "Rarefaction Waves in Liquid and Gas-Liquid Media," *Annual Review of Fluid Mechanics*, Vol. 19, 1987, pp. 577–600.

[22]Fergason, S. H., Ho, T., Argrow, B. M., and Emanuel, G., "Theory for Producing a Single-Phase Rarefaction Shock Wave in a Shock Tube," *Journal of Fluid Mechanics*, Vol. 445, 2001, pp. 37–54.

[23]Martin, J. J., and Hou, Y., "Development of an Equation of State for Gases," *AIChE Journal*, Vol. 1, No. 2, 1955, pp. 142–151.

[24]Thompson, P. A., "Liquid–Vapor Adiabatic Phase Changes and Related Phenomena," *Nonlinear Waves in Real Fluids*, edited by A. Kluwick, Springer-Verlag, Berlin, 1991, pp. 147–213.

[25]Fergason, S. H., and Argrow, B. M., "Simulations of Nonclassical Dense Gas Dynamics," AIAA Paper 2001-2752, June 2001.

[26]Figliola, R. S., and Beasley, D. E., *Theory and Design for Mechanical Measurements*, Wiley, New York, 2000, pp. 149–191.

[27]Holman, J. P., *Experimental Methods for Engineers*, 5th ed., McGraw–Hill, New York, 1989, pp. 37–91.

[28]"Operating Instructions: Water-Cooled ThermoCOMP Type 7061B Pressure Sensors," Product Specifications Document No. B03.7061B1e-04.99, Kistler Instruments, Winterhur, Switzerland, 2000.

[29]"Operating Instructions: Water-Cooled ThermoCOMP Type 4043A Pressure Sensors," Product Specifications Document No. B3.03le-5.80, Kistler Instruments, Winterhur, Switzerland, 2000.

[30]Alpher, R. A., and White, D. R., "Flow in Shock Tube with Area Change at the Diaphragm Section," *Journal of Fluid Mechanics*, Vol. 3, 1958, pp. 457–470.

[31]White, D. R., "Influence of Diaphragm Opening Time on Shock Tube Flows," *Journal of Fluid Mechanics*, Vol. 4, 1958, pp. 585–599.

[32]Rothkopf, E. M., and Low, W., "Diaphragm Opening Process in Shock Tubes," *Physics of Fluids*, Vol. 17, No. 6, 1974, pp. 1169–1173.

[33]Hickman, R. S., Farrar, L. C., and Kyser, J. B., "Behavior of Burst Diaphragms in Shock Tubes," *Physics of Fluids*, Vol. 18, No. 10, 1975, pp. 1249–1252.

[34]Petrie-Repar, P., and Jacobs, P. A., "A Computational Study of Shock Speeds in High-Performance Shock Tubes," *Shock Waves*, Vol. 8, No. 2, 1998, pp. 79–91.

[35]Guardone, A., and Quartapelle, L., "Spatially Factorized Galerkin and Taylor–Galerkin Schemes for Multidimensional Conservation Laws," Dipartimento di Ingegneria Aerospaziale, Scientific Rept. DIA-SR 00-18, Politecnico di Milano, Milan, Italy, 2000.

[36]Selmin, V., "The Node-Centred Finite Volume Approach: Bridge Between Finite Differences and Finite Elements," *Computer Methods in Applied Mechanics and Engineering*, Vol. 102, No. 1, 1993, pp. 1–32.

[37]Roe, P. L., "Approximate Riemann Solvers, Parameter Vectors, and Difference Schemes," *Journal of Computational Physics*, Vol. 43, No. 2, 1981, pp. 357–372.

[38]Selmin, V., and Formaggia, L., "Unified Construction of Finite Element and Finite Volume Discretizations for Compressible Flows," *International Journal of Numerical Methods in Engineering*, Vol. 39, No. 1, 1996, pp. 1–32.